ARTICLE

Check for updates

Untethered and ultrafast soft-bodied robots

Xu Wang [1,4], Guoyong Mao[2,3,4], Jin Ge[1], Michael Drack[2,3], Gilbert Santiago Cañón Bermúdez[1], Daniela Wirthl[2,3], Rico Illing[1], Tobias Kosub[1], Lothar Bischoff[1], Changan Wang[1], Jürgen Fassbender[1], Martin Kaltenbrunner[2,3✉] & Denys Makarov [1✉]

Acting at high speed enables creatures to survive in their harsh natural environments. They developed strategies for fast actuation that inspire technological embodiments like soft robots. Here, we demonstrate a series of simulation-guided lightweight, durable, untethered, small-scale soft-bodied robots that perform large-degree deformations at high frequencies up to 100 Hz, are driven at very low magnetic fields down to 0.5 mT and exhibit a specific energy density of 10.8 kJ m^{-3} mT^{-1}. Unforeseen asynchronous strongly nonlinear cross-clapping behavior of our robots is observed in experiments and analyzed by simulation, breaking ground for future designs of soft-bodied robots. Our robots walk, swim, levitate, transport cargo, squeeze into a vessel smaller than their dimensions and can momentarily close around a living fly. Such ultrafast soft robots can rapidly adapt to varying environmental conditions, inspire biomedical applications in confined environments, and serve as model systems to develop complex movements inspired by nature.

[1] Helmholtz-Zentrum Dresden-Rossendorf e.V., Institute of Ion Beam Physics and Materials Research, Bautzner Landstrasse 400, 01328 Dresden, Germany. [2] LIT Soft Materials Lab, Linz Institute of Technology, Johannes Kepler University Linz, Altenberger Strasse 69, 4040 Linz, Austria. [3] Division of Soft Matter Physics, Institute for Experimental Physics, Johannes Kepler University Linz, Altenberger Strasse 69, 4040 Linz, Austria. [4] These authors contributed equally: Xu Wang, Guoyong Mao. ✉email: martin.kaltenbrunner@jku.at; d.makarov@hzdr.de

Acting at high speed is essential to creatures in nature for preying, fleeing, and flying, examples include fast running cheetahs and flying hummingbirds with a wing-beat rate of 80 times per second. High speed is equally desirable in soft robotics as it enables gripping fast-moving objects and quickly responding to their dynamic surroundings[1–3]. Unlike conventional hard-bodied robots that are usually driven by electric motors, their soft counterparts are based on functional soft materials[4,5] such as dielectric elastomers[6–8] or shape-memory[9–11], chemically sensitive[12,13], and magnetically functionalized polymers[14–22]. The magnetic field is a promising driving force that potentially enables fast actuation[16,23,24] remotely without constraining on-board power sources and control units typically required for untethered robots[25,26]. Such soft robots can be programmed during fabrication[14,16–22,27–31], enabling them to accomplish various tasks. These properties endow magnetic soft robots with the ability to move even in complex environments for biomedical applications such as cell manipulation[21], drug delivery[32], and disease diagnosis[33–35].

In real applications, fast actuation may help such magnetic soft robots to persist long enough to work in harsh operational areas with complex and adaptive environments. However, current magnetic soft robots are limited by their actuation speed (<30 Hz[16]) and specific energy density (<4 kJ m^{-3} mT^{-1},[22]) and so far, only respond monotonously to the external driving magnetic field[16,18,19,21,22], rendering unconventional locomotion that exploits nonlinearities inaccessible. A set of high-performance materials and new fabrication methods in combination with high speed, nonlinear dynamic analysis is required to unlock advanced functionalities of magnetic soft robots. Existing computational methodologies allow structural optimizations of soft magnetic robots, but do not allow to determine the time-varying shapes of soft magnetic robots when the driving magnetic field is time-invariant because of the highly nonlinear behavior of such soft structures[20]. Even more advanced soft-bodied magnetic jellyfish[16] are described phenomenologically but not modeled predictively, eventually limiting further developments of such biologically inspired robots.

Here, we demonstrate lightweight, durable (>2 million actuation cycles without failure), untethered, small-scale soft-bodied robots performing large-degree deformations at high frequencies up to 100 Hz that are driven at very low magnetic fields down to 0.5 mT and exhibit a high specific energy density of 10.8 kJ m^{-3} mT^{-1}. The high specific energy density, thin and lightweight design of our robots allow them to operate at a low magnetic field and high frequencies and where complex dynamics set in and unlock previously unknown behavioral patterns. We tailor the excitation frequency to switch deterministically among qualitatively different forms of motion. We demonstrate a crossover from linear to highly nonlinear and even resonant behavior of the mechanical system, which triggers the transition from trivial deformation to sophisticated cross-clapping motions, and develop a numerical model aiding the fundamental understanding of these complex dynamics in ultrafast soft robots. Explicitly, we focus on the cross-clapping motion where nonlinear mechanics of magnetic soft robots set in. These nonlinearities might be considered as a disadvantage as the motion of a soft robot can become unpredictable and hence difficult to be controled. However, we here demonstrate that even in this regime, soft robots can be not only precisely controlled but also can accomplish unusual motion patterns exemplified with cross-clapping motion. Our soft-bodied robots walk, swim, levitate, transport cargo, and can be fast enough to close around a living fly. This inspires new classes of soft robots that impact biological tissue engineering, confined and high-speed mechanical tissue manipulation, and serve as working models to study fast biomechanical processes like hydro- and aero-dynamics of fast-moving organisms.

Results and discussion

Fabrication and characterization of magnetic soft-bodied robots. To explore different behavioral patterns, we here introduce materials and design rules to realize ultralight soft robots based on spin-coated elastomers (polydimethylsiloxane, PDMS) with a high amount of magnetic neodymium-iron-boron (NdFeB) microparticles with an average diameter of 5 μm. To define their magnetic states, the as-casted composites are magnetized in an out-of-plane magnetic field of 2.3 T (Fig. 1a). By shaping our thin magnetic membranes into different geometries (e.g., 2-, 3-, 4-, 5-arm) (Fig. 1a, b) using frugal and high throughput patterning methods such as stencil cutting, various unusual robot motion modes are achieved. Our robots perform remotely in air driven by a very small magnetic field (<2 mT) that is generated by a pair of coils (Fig. 1c). The robot movements are defined by the applied magnetic field, the robot weight, and the magnetization of the magnetic elastomer membrane. Applying a horizontal magnetic field (in the plane of the relaxed soft robot) to a two-arm robot, for example, actuates its right arm (Fig. 1c). The largest size of our magnetic soft robots is only limited by the space and amplitude of the magnetic field, and homogeneity of the magnetic elastomer fabricated by spin coating. The smallest size of our robots is constrained by the thickness of the magnetic membrane that should be larger than the diameter of the magnetic particles (5 μm in our study). A large magnetic field in an extended space necessitates an energy-demanding electromagnet. Therefore, favorable and economical magnetic soft robots with miniature dimensions are of high relevance to reduce the field amplitude required for their actuations. Moreover, thin and lightweight membranes with a high magnetization are essential to achieve large deformations at high speeds. The thickness of the magnetic membrane is controlled by the spin-coating speed (Supplementary Fig. 1a). We here reliably achieve minimum membrane thicknesses as thin as 7 μm using a high spin-coating speed (12,000 rpm) and peel it off from the substrates using a water dissolvable sacrificial layer of polyvinyl alcohol (PVA). Maximizing the mass ratio of the magnetic filler (NdFeB powder) within the PDMS/NdFeB composite elastomer without compromising flexibility is the key to achieve high-performance actuation.

We show that a loading weight ratio of 70% NdFeB particles results in remanent and saturation magnetizations of about 123 and 170 kA m^{-1}, respectively (Supplementary Fig. 1b) with a calculated mass density for such a magnetic elastomer of around 2.13 × 10^3 kg m^{-3} (Supplementary Fig. 1c).

The 70 wt% particles loading increases the stiffness of the robots[37,38] and provides a larger Young's modulus up to 4.9 ± 0.2 MPa (Supplementary Fig. 1d), which also benefits the applications that demand strong mechanical properties of the robot. We actuate a 7-μm-thin rectangle-shaped robot (lateral dimensions: 5 × 10 mm^2) in water by using a square magnetic field profile (0.5 mT, 2 Hz) (Supplementary Fig. 2a and Supplementary Movie 1). In the following experiments and simulations, unless otherwise noted, we use driving magnetic fields in the form of a square wave (Supplementary Fig. 2a). Moreover, our five-arm robots achieve full 90° actuation by an in-plane magnetic field (only 2 mT) in air (Supplementary Fig. 3a). Even an in-between 2.5-cm-thick nontransparent obstacle does not decrease the actuation performance (Supplementary Fig. 3b). The calculated maximum energy density of 21.7 kJ m^{-3} is among the highest values of magnetic soft robots to date (Fig. 1d). Crucial for high-speed actuation at low external magnetic fields is the specific energy density, where our soft robots reach up to 10.8 kJ m^{-3} mT^{-1}, far beyond what was previously achieved (Fig. 1d)[15,16,18,19,22,36]. We develop a dynamic numerical model to capture the unexpected nonlinear dynamics of our ultrafast
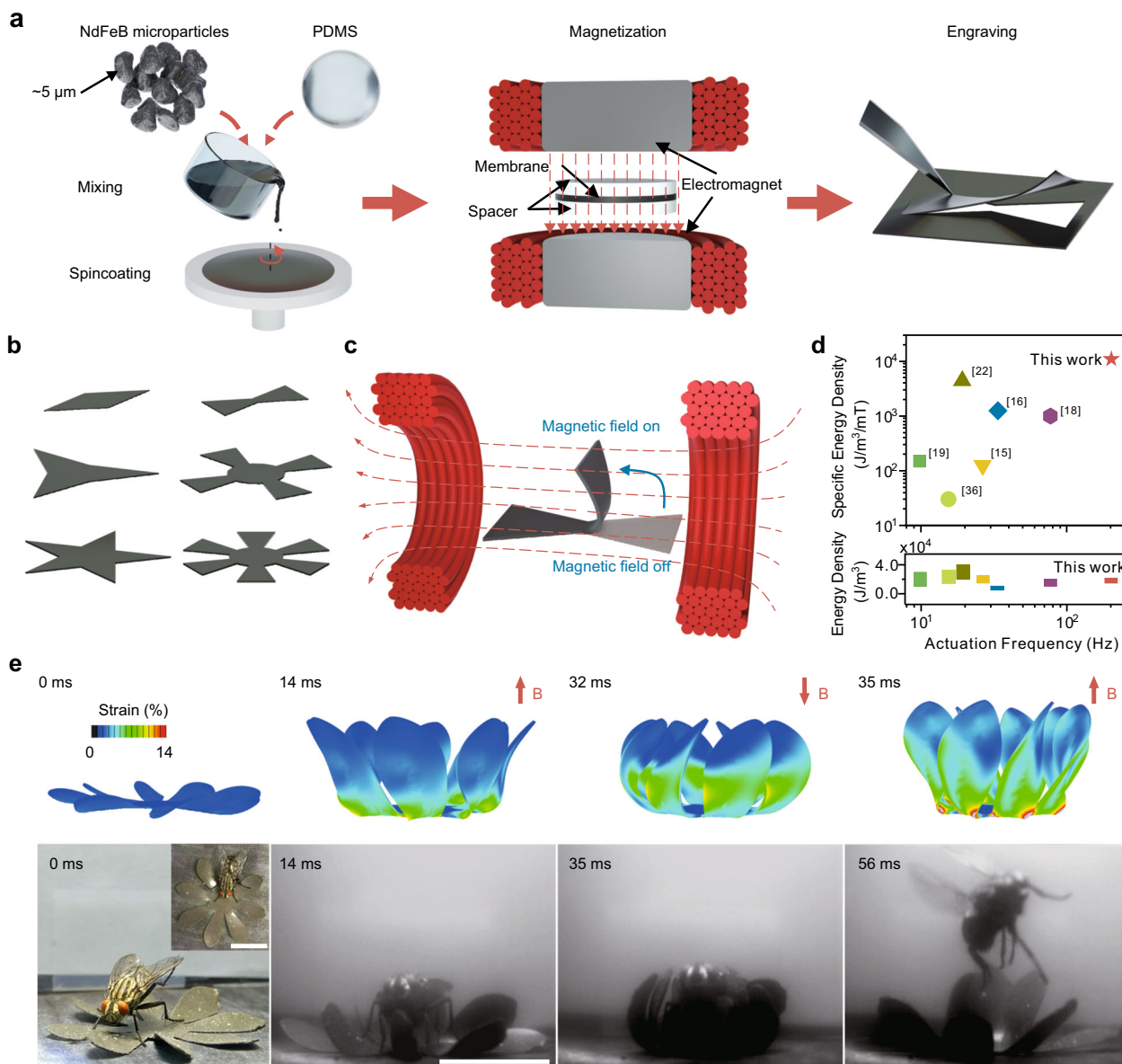
Fig. 1 Ultrafast, lightweight, and resilient magnetic soft-bodied robots. a Illustration of the preparation steps for NdFeB/PDMS membrane-based magnetic soft robots. A magnetic composite is fabricated by mixing NdFeB microparticle fillers with PDMS at high loading ratios of 70 wt% magnetic solids. Subsequent spin-coating yields thin (down to 7 μm) elastomeric membranes that are magnetized by an out-of-plane magnetic field induced by an electromagnet. A ready-to-use magnetic soft robot is obtained by high throughput engraving or cutting of the magnetic membranes. **b, c** Schematic diagram showing different types of multi-arm robots, as well as the setup (two electromagnetic coils) used to achieve untethered robot actuation. **d** Performance (energy density and specific energy density) of our magnetic soft robots compared to other approaches[15,16,18,19,22,36]. **e** Simulated (top row) and experimental (bottom row) results of a flower-shaped magnetic soft robot highlight the predictive nature of our dynamic model and the versatile applicability of the robot due to its fast and silent actuation. It closes around a living fly momentarily and releases it again without harming the fragile insect (Supplementary Movie 2). Scale bars, 1 cm.

magnetic soft robots that we here observe for the first time experimentally (Fig. 1e). It allows us to not only describe the peculiarities of such asynchronous strongly nonlinear responses as illustrated here for the cross-clapping behavior, but also to predict unusual motion patterns.

The unique characteristics of our magnetic elastomer membranes enable our robots to achieve ultrafast actuation with large deformations even superior to natural processes. We design a flower-shaped robot (thickness: 210 μm, diameter: 2.5 cm, Fig. 1e) that is fast enough to close around a fly momentarily before it registers the closing trap. To avoid deformations of the magnetic elastomer during the magnetization procedure, we bond the

gripper on a glass substrate using a double-sided tape. To actuate the robot, we use a magnetic field of 3 mT at 50 Hz (Supplementary Fig. 4). An actuation frequency higher than 10 Hz, as well as an actuated rotation angle larger than 90°, is essential for this process as the natural reaction times of flies are around 100 ms[39]. The numerical simulation shows that it takes around 35 ms to fully close our flower-shaped robot when being actuated by an out-of-plane magnetic field of 3 mT at 50 Hz. The robotic closing motion is around eight times faster than similar processes in nature like the closing of a Venus Flytrap as validated experimentally (Fig. 1e and Supplementary Movie 2). The inverse reopening procedure takes 25 ms (Supplementary Fig. 5 and

Supplementary Movie 2), which outperforms a Venus Flytrap (1 day[40]) by several orders of magnitude in speed.

Despite fast response, our soft robot maintains a durable and stable actuation performance even after more than 2 million actuation cycles (Supplementary Fig. 6). When constantly actuating a two-arm robot in a 2 mT field at 20 Hz, the speed of deformation of one single arm from 0 to 90° is around $7.5° \, ms^{-1}$. Cyclic endurance tests show stable actuation of the robot arm without loss of performance (Supplementary Fig. 6 and Supplementary Movie 3).

Dynamic performance of one-arm soft robots. The synchronous response frequency of soft robots can be improved up to 200 Hz by increasing the driving frequency of the magnetic field. A good agreement between experimental and simulated results of an one-arm triangle-shaped robot (lateral dimensions: $4 \times 7.5 \, mm^2$; thickness: 80 μm) actuated by a horizontal square wave magnetic field (4 mT, 60 Hz, the field profile is shown in Supplementary Fig. 2b) validates our numerical model (Fig. 2a and Supplementary Movie 4). When the amplitude of the magnetic field is fixed to 4 mT, a two-arm rectangle-shaped robot can perform 90° rotation at a driving frequency of up to 80 Hz (Supplementary Fig. 7 and Supplementary Movie 5). The driving frequency for 90° rotation can be further improved up to 100 Hz by increasing the amplitude of the magnetic field to 9 mT (Fig. 2b, Supplementary Fig. 8, and Supplementary Movie 5). A summary of these experimental results is given in Supplementary Fig. 9. We further show that the actuation frequency can even be increased to 200 Hz (deterministic actuation), yet the maximum rotation angle then is limited to 45° because of the low amplitude of driving magnetic field (2 mT) (Supplementary Fig. 10 and Supplementary Movie 5).

To inform future soft robot design, a clear understanding of the smallest unit dependent motion pattern that forms assembled robots is mandatory. One-arm actuation is reported as a fundamental building block for a majority of soft robots[41,42]. Therefore, we carry out numerical studies of the influence of the geometry of each arm (trapezoid, rectangle, and triangle) (Supplementary Fig. 11), the driving frequency of the magnetic field (10–200 Hz), as well as the thickness of the robot (100–1000 μm) on the dynamic response. We analyze the schematic diagram of a one-arm robot bending from 0° to 310° driven by a horizontal square wave magnetic field (Fig. 2c).

The driving force originates from the magnetic torques of the embedded magnetic fillers inside the magnetic elastomer (the transition direction of the magnetic torque (m) and the magnetization (M) is shown in Fig. 2c). If the direction of the magnetic field B is constant, the magnetic torque m at the tip of the robot arm switches from counterclockwise (CCW) to clockwise (CW) when the rotation angle is beyond 90° (Fig. 2c). Therefore, to accomplish a full close or obtain larger deformations, there is a need to change the direction of the magnetic field when the rotation angle is over 90°. The simulation reveals that it takes about 25 ms for the robot to rotate from 0° to 90°, which refers to an optimal actuation frequency of around 20 Hz to accomplish a full close ($\alpha > 270°$) (Fig. 2d). For a high driving frequency (e.g., 50 Hz), the maximum rotation angle during the first period is about $\beta \sim 78°$, then the rotation angle firstly decreases, and increases again to an even higher value ($\gamma \sim 173°$) which is similar to a relay race (Fig. 2e). Such a relay race only happens at a certain range of frequencies, for example, from 31 to 95 Hz in the case of a trapezoid-shaped robot as visible in Fig. 2f, g. We also find that under low frequencies such as 20 Hz, the robot goes back to its initial position (Fig. 2d), but under higher frequencies (e.g., 50 Hz) it starts trembling (Supplementary

Movie 6) as validated experimentally. Compared to other robot designs such as triangle and rectangle in shape, the trapezoid geometry yields the largest maximum rotation angle when driven at low frequencies, and therefore it becomes easier to achieve large actuated deformation (Fig. 2f, g). Our model further indicates that distributing more material on the tip of the robot arms would enhance the inertial effect and the magnetic torque of the robot, resulting in larger maximum rotation angles at the same load. Calculations using the maximum actuation strain (obtained from simulations) yield a maximum energy density of $80 \, kJ \, m^{-3}$ and a power density of $2.47 \, mW \, m^{-3}$ (Supplementary Fig. 12). The simulation shows peak values for maximum strain, energy density, and power density at ~25 Hz with lower constant values for frequencies beyond 50 Hz. A one-arm trapezoid-shaped robot driven by a square wave magnetic field (2 mT, 200 Hz) reaches a maximum deformed angle of 19° at a maximum strain of 5.9% and yields maximum energy and power densities of $1.27 \, kJ \, m^{-3}$ and $0.253 \, MW \, m^{-3}$, respectively. We further study by simulation how the bending motion is affected by the thickness of the robot. The bending stiffness of a one-arm robot is proportional to the cube of its thickness and the magnetic moment is linearly proportional to the thickness of the soft robots. Decreasing the thickness of the soft robots from 1000 to 100 μm reduces the magnetic moment by 90% of its original value, which also decreases the deformed area of the soft robot. To indicate this effect, we evaluate the active length, defined as the length of the deformed part of the robot exposed to a certain magnetic field. We numerically analyze the active length of magnetic elastomer beams with different thickness subjected to a series of magnetic fields ranging from 0 to 4 mT (Supplementary Fig. 13a). The results of the simulations show that the active length increases for the case of thicker robots and stronger magnetic fields. It is, for example, 27 mm for a 100-μm-thick beam, and 36 mm for a 1000-μm-thick one. The larger rotation angle of the thinner robot also validates the result. While a 100-μm-thick robot can be bent to 90° in a 2 mT magnetic field, a 4 mT magnetic field is needed to achieve a similar rotation angle for a 562-μm-thick beam (Supplementary Fig. 13b). Therefore, decreasing the thickness of the robot is a feasible way to speed up the response of the robot. Simulations of a one-arm trapezoid-shaped robot (Supplementary Fig. 14) with different thicknesses from 100 to 1000 μm performing at the same load condition (Fig. 2f, g) indicate that above a certain thickness (in our case larger than 400 μm) mechanical resonance vanishes. Decreasing the thickness leads to a substantial increase of the maximum rotation angle under the same load. In our simulation, the maximum rotation angles in one period are 272, 152, 85, and 54 degrees for soft robots with a thickness of 100, 400, 700, and 1000 μm, respectively.

Even though thinner robots are easier to be bent by magnetic fields, they still fail to accomplish a standard bending when the size is enlarged above a certain threshold. Here, the expression "standard bending" is used to indicate that upon actuation, the active length is equal to the body length and the shape of the robot is close to an arc (Fig. 2a). We use such triangle-shaped robots driven by a square wave magnetic field (4 mT) to analyze failure modes. We study three differently sized robots (bottom length × height), type I ($5 \times 8 \, mm^2$), type II ($10 \times 16 \, mm^2$), and type III ($20 \times 32 \, mm^2$), which are also prepared with three different thicknesses, 45, 85, and 180 μm. We identify two main failure modes: one is collapse; a typical process is shown in Supplementary Fig. 15a. It occurs when the driving frequency is low (Supplementary Fig. 15b–d). A second failure mode, referred to as partial bending with the active length (5 mm) being smaller than the body length (32 mm) of the robot, is observed at high driving frequencies (Supplementary Fig. 15e). We further analyze
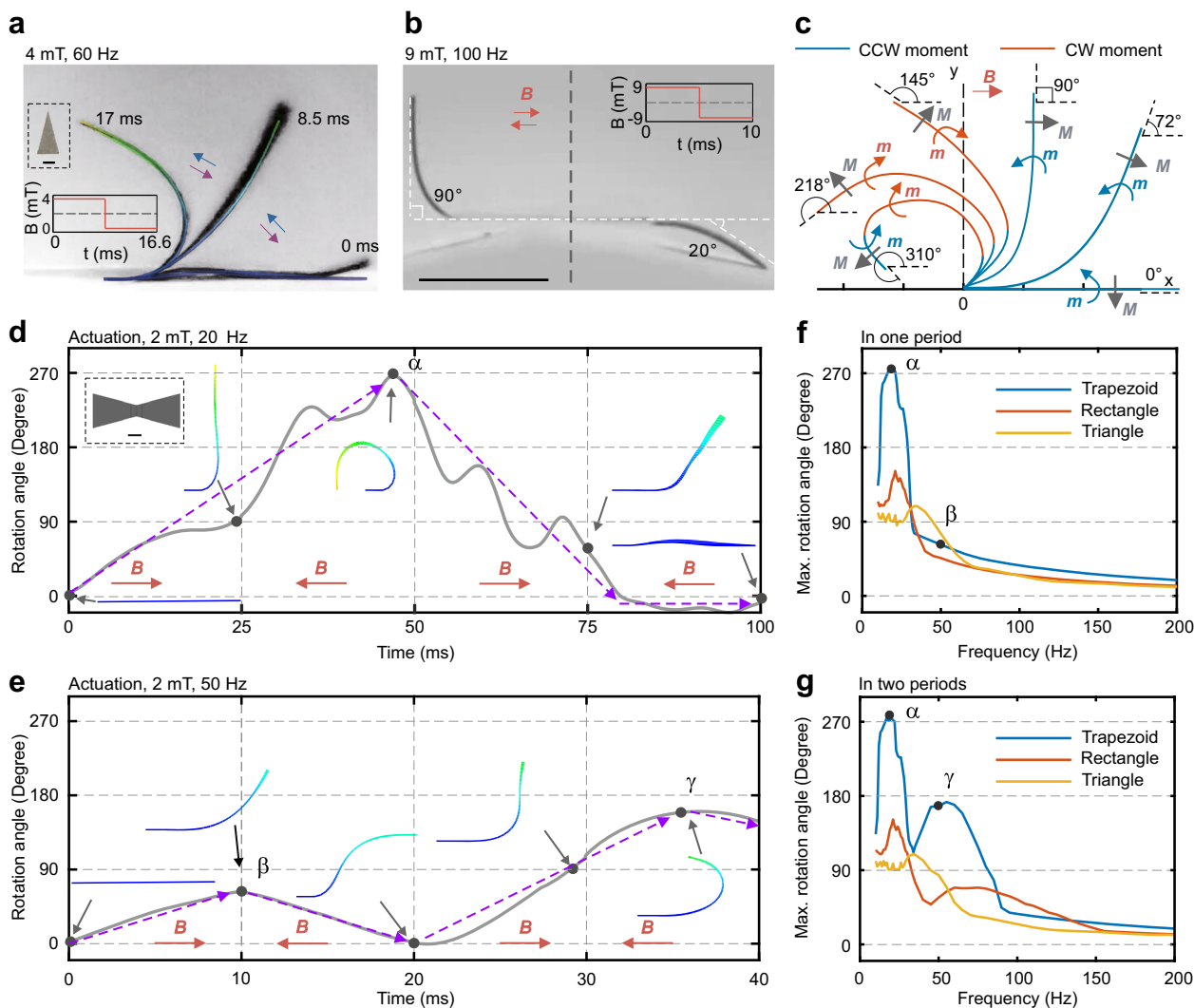
Fig. 2 Dynamics and actuation performance of a magnetic soft robot. a Experimental and simulated snapshots present one actuation period of a one-arm triangle-shaped robot driven by a square wave magnetic field (4 mT, 60 Hz, shown in the inset or the form as Supplementary Fig. 2b) (Supplementary Movie 4). One end of the robot is fixed on a substrate. **b** Experimental snapshot revealing 90° deformation of a two-arm rectangle-shaped robot (lateral dimensions: 6×0.8 mm^2, thickness: 45 µm) at a driving frequency of 100 Hz when the amplitude of the magnetic field is 9 mT (square wave). See also Supplementary Fig. 8 and Supplementary Movie 5. The middle point of the robot is fixed on a curved substrate. **c** Direction of magnetization M and magnetic torque m of a one-arm triangle-shaped robot during actuation as shown in (**a**). **d**, **e** Time-dependent rotation angle during the actuation of a one-arm trapezoid-shaped robot driven by a square wave magnetic field (2 mT) at 20 and 50 Hz, respectively. Maximum rotation angles are highlighted with Greek letters: α is the maximum rotation angle achieved at 20 Hz, β at 50 Hz for one period, and γ at 50 Hz for two periods. The purple lines indicate the trend of the variation of the angle. **f**, **g** Calculated frequency-dependent maximum rotation angles of differently shaped robots for one and two periods driven by a square wave magnetic field (2 mT), respectively. Scale bars, 0.2 cm.

the effects of the driving frequency, size, and thickness on the failure modes of the robots. Both failure mechanisms (collapse and partial bending) of these soft robots are also captured in simulations (Supplementary Fig. 15f), in which the extracted midline of the robot is shown in Supplementary Fig. 15g. The experimental results show that the collapse appears more often when the robot is driven at lower frequencies, for thinner robots, and robots with larger lateral dimensions (Supplementary Fig. 15h). This experimental finding is in line with the simulation results. In addition, we utilize three parameters to analyze the failure modes of the robot in the simulations (Supplementary Fig. 15i–k). The first parameter is the maximum displacement of the robot's tip along the y-axis, Max. y_{tip}, divided by the body length H_0. The second one is the maximum number of folds during the bending, Max. n_f. The third parameter is the standard error of maximum displacement in the z-axis, z_{max}, of each

material point on the midline divided by the corresponding $\times$ coordinates. We find that a Max. $y_{tip}/H_0 > 0.2$ or the Max. $n_f > 1$ can induce collapsed motion. A ratio of z_{Max}/x_0 larger than 0.1 results in a higher possibility of partial bending. This analysis is performed for a constant amplitude of the magnetic field. Similar to the buckling process of a beam, with the increase of the field amplitude, the robot becomes more susceptible to buckling and hence collapses. For the case of partial bending, increasing the field amplitude might be a promising route to overcome this failure. We note that the above analysis also shows that the maximum rotation angle, which is extracted at the tips of the robots (Fig. 2f, g), slightly overestimates the amplitude of bending of the entire robot at higher driving frequencies (e.g., 100 Hz) when partial bending occurs. The above analysis indicates that the typical lateral dimensions of our robots should be in the range from millimeter to centimeter.
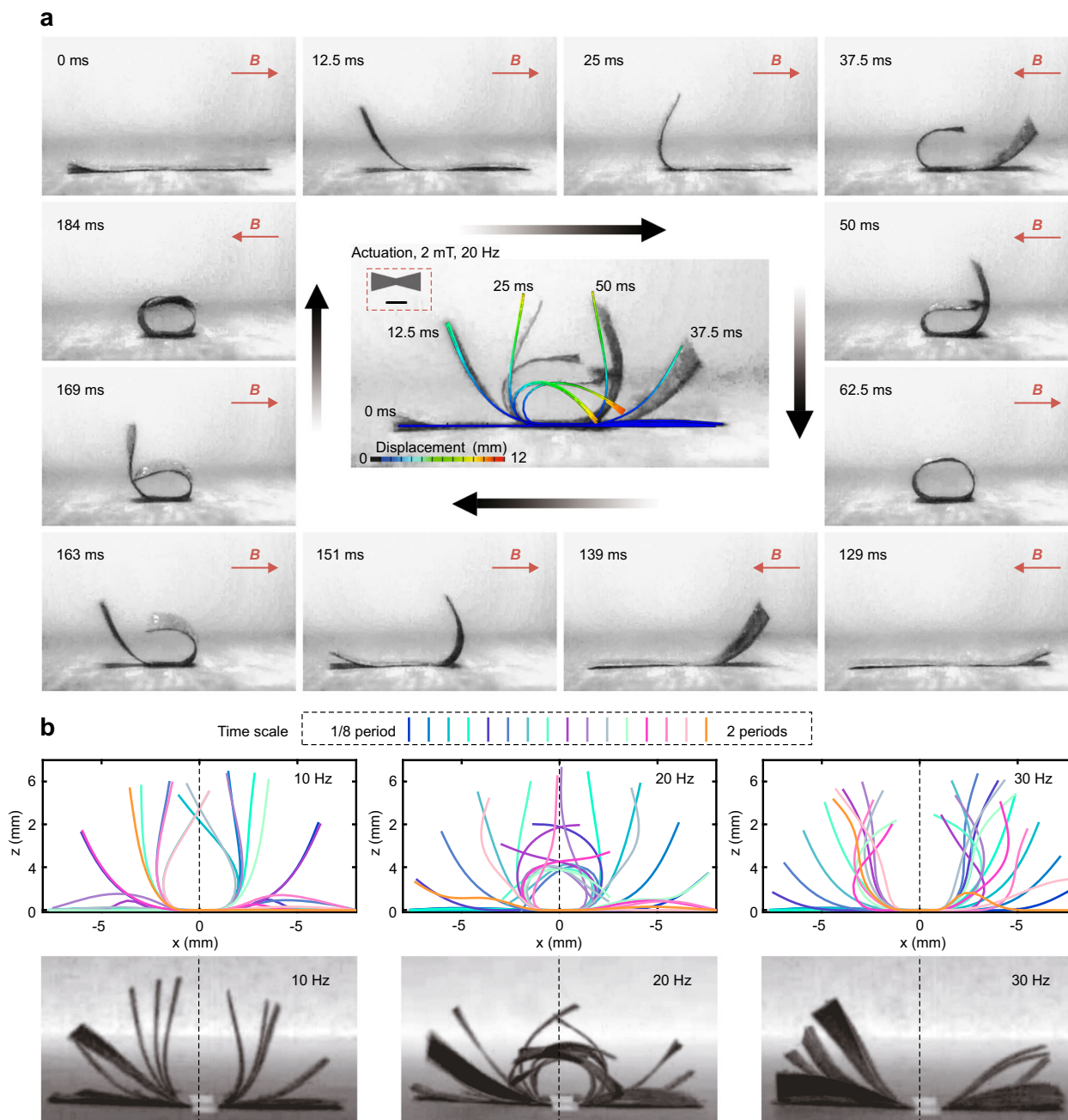
Fig. 3 Asynchronous strongly nonlinear dynamic actuation of a two-arm trapezoid-shaped soft robot. a Experimental and simulated robot actuation triggered by a magnetic field at 20 Hz (Supplementary Movie 7). The central figure shows the traces of the actuation predicted by the simulation compared to the experimentally observed ones. The surrounding panels show the dynamics of the soft robot actuation for one full period. **b** Comparison of the simulated with the experimental results of a two-arm robot actuation triggered by magnetic fields at 10, 20, and 30 Hz, respectively. Cross clapping is allowed only for frequencies close to 20 Hz. For these experiments, the middle point of the robot is fixed on a substrate. Scale bars, 0.5 cm.

Asynchronous strongly nonlinear cross clapping of a two-arm soft robot. The simulation of the two-arm bow-tie-shaped robot predicts a fast, repeatable, and precisely controlled motion pattern upon square wave magnetic field actuation (20 Hz), which is distinct from trivial bending. This pattern is akin to a cross-clapping motion of a human (colored lines in Fig. 3a). In this experiment, we apply a regular alternating magnetic field, however, the robot responds in an unconventional and unexpected fashion. Usually, the robot sequentially moves its left and right arms following the period of the magnetic field. Upon performing the cross-clapping motion, the robot bends its left arm followed by the bending of its right arm and then continues to unfold the right arm while the left

arm remains bent (delayed response with respect to the actuation sequence). Such cross-clapping motion is asynchronous strongly nonlinear compared to the existing soft robots. We provide a schematic figure to illustrate the difference of different motion patterns (Supplementary Fig. 16). The snapshots of the motion trajectory in Fig. 3a show the cross-clapping movement sequence in detail (Supplementary Movie 7). The robot lays flat on the substrate initially, and then the left arm bends from 0° to 82° in 25 ms, while the right arm does not respond when the magnetic field (2 mT, 20 Hz) is applied. Next, the right arm starts to deform to 75.8° until 50 ms, touching the tip of the left arm, which continuously bends to 180° at the same time. The right arm completes its movement until
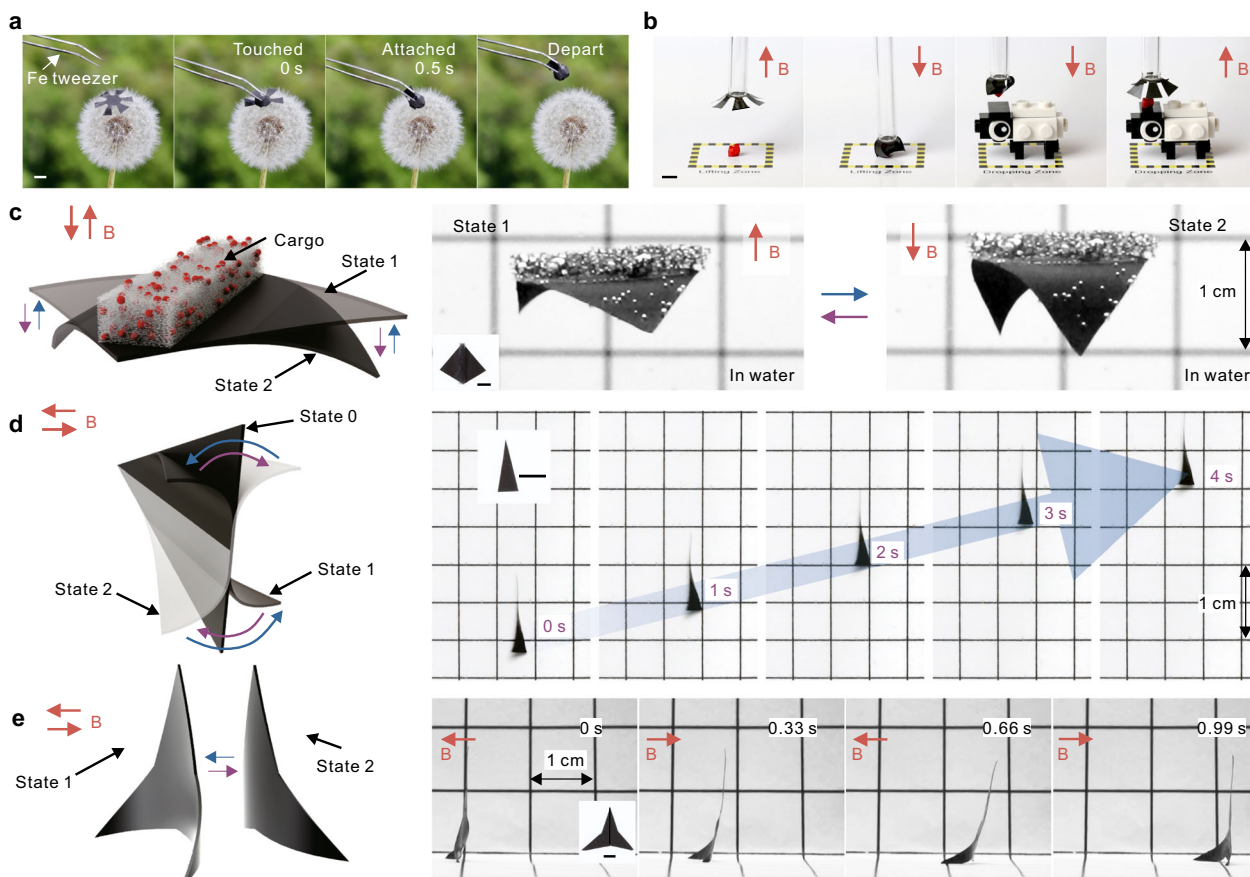
Fig. 4 Ultrafast soft robots that self-attach, transport cargo, and swim. a A six-arm robot on a dandelion can self-grip when approaching magnetic tweezers without harming the fragile structure of the flower (Supplementary Movie 9). **b** The same robot can also grab, transport, and release nonmagnetic objects such as a polyurethane foam cube controlled by a permanent magnet (Supplementary Movie 10). **c** Manta ray-shaped robot with a cargo swimming in water (Supplementary Movie 11). **d** Triangle-shaped swimming robot twisting around its main axis and therefore moving forward in the water, both driven by a square wave magnetic field (Supplementary Movie 12). **e** Triangle-shaped walking robot rolling itself in air at high speeds when subjected to an alternating magnetic field (Supplementary Movie 13). Scale bars, 0.5 cm.

it rests perfectly on the left arm (62.5 ms). Afterward, the recovery movement starts and brings the two arms back to the initial flat-lying position, followed by another round of cross clapping with switched motion sequences. The actuator performs a so-called "mirroring action" repeating the motion by switching the movements of the left and right arm. After the second recovery sequence, the actuator has performed a full round of cross clapping (Supplementary Movie 7). The mechanism of cross clapping is presented in Fig. 3b. Our analysis reveals that the actuated frequency should be around 20 Hz to achieve a full close of a one-arm robot (bending angle > 270°).

The simulated response of the bow-tie-shaped robot to magnetic fields with frequencies ranging from 10 to 30 Hz (Supplementary Fig. 17) indicates that the two robot arms touch each other only at the frequencies between 13 and 27 Hz, among which only certain frequencies enable the robot to accomplish the cross-clapping behavior (around 20 Hz). The simulated and experimental traces of the cross-clapping motion at 10, 20, and 30 Hz are shown in Fig. 3b. When the frequency of the magnetic field is close to 13 or 27 Hz and far away from 20 Hz, the first touch happens in the area close to the tip of the arms, and hence they cannot overlap (Fig. 3b and Supplementary Movie 8).

Versatile functions of soft robots. Instead of magnetic coils, our robots also can be driven by permanent magnets enabling more

flexibility and convenience for everyday usage. The thin and lightweight design allows working possibilities without inducing any harm on delicate surfaces such as the head of a dandelion. When approaching magnetic tweezers, the gentle robot is attracted to the metal and wraps its arms around the tip of the tweezers until it is fully holding its weight (Fig. 4a and Supplementary Movie 9). The robot can operate on a bumpy or even rough surface such as on the top of a very sharp cactus spine without rupture, being a further benefit of the lightweight and resilient design (Supplementary Fig. 18). Our six-arm robot also operates as a soft gripper, transporting, and releasing objects (Fig. 4b). To do so, the robot is fixed on a glass stick in its open state firstly. Changing the direction of the magnetic field induces bending of the arms until it grips a cubic polyurethane foam. As the robot retreats from its initial position or approaches another magnet with a reversed magnetic field, it opens again and releases its payload (Supplementary Movie 10).

We design two robots with different motion modes swimming in water (Supplementary Movies 11 and 12). The modeling dynamics of the first one, a manta ray-shaped robot, indicate that an actuation of the two robot arms between −90° and 90° imitating the fin movement of its natural antetype is achievable with an out-of-plane square wave magnetic field (2 mT, 1 Hz) (Supplementary Fig. 19 and Supplementary Movie 11). The experimental results (Fig. 4c) illustrate the functionality of our manta ray-shaped robot design that is even able to carry payloads.
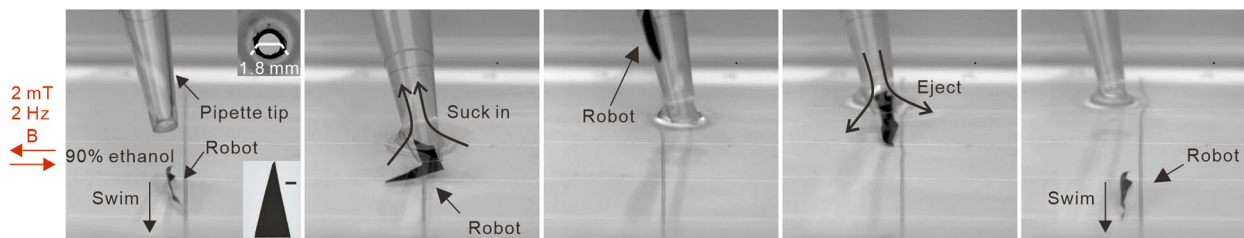
Fig. 5 Highly conformal ultrathin magnetic soft robots. A triangle-shaped magnetic soft robot (lateral dimensions: 12 × 5.8 mm²; thickness 45 μm) can be inserted in/released from a pipette tip with an opening of 1.8 mm in diameter. The magnetic manipulation allows the robot to minimize its cross-section, which enables its insertion into the pipette (Supplementary Movie 14). The robot is driven by a square wave magnetic field (2 mT, 2 Hz). Scale bar, 2 mm.

The movement of its two fins creates a strong thrust that allows the robot to glide forward in water. We note here that the payload also plays a role to balance the robot and prevents body rotation during swimming. The second type of swimming robot is based on a slim triangular design, moves forward by rotating around its own axis similar to the motion of a propeller, and achieves high-speed locomotion in water (Fig. 4d, snapshots in Supplementary Fig. 20, and Supplementary Movie 12).

With an upright standing three-arm robot, we demonstrate forward-backward walking movement in air at a speed of 18 cm s⁻¹ exploiting fast self-rolling (Fig. 4e, snapshots in Supplementary Fig. 21, and Supplementary Movie 13). As the weight of the robot is just 10 mg, it can stand up in 0.4 s and lay down again in 0.42 s when actuated by a magnetic field (3.5 mT, 1.5 Hz). Meanwhile, the magnetic field gradient induces the walking displacement of the robot in the desired direction.

To showcase the practical relevance of the high compliance of our robots, we demonstrate insertion and release of a triangle-shaped swimming robot into a narrow syringe when manipulated by a magnetic field (2 mT, 2 Hz; Fig. 5, Supplementary Movie 14). Primarily, the ultrathin design provides a high degree of freedom to the untethered body deformation of the robots. This feature enables them to pass through channels with an opening smaller than their lateral dimensions. We illustrate this by inserting a rather large (lateral dimensions: 12 × 5.8 mm²; thickness 45 μm) triangle-shaped swimming robot into a pipette tip with an opening of 1.8 mm in diameter. Upon insertion, the robot wraps itself to minimize its cross-section. When needed, the robot can be released from the pipette in ethanol solution and continue swimming. Upon this manipulation, the robot fully recovers its initial dimensions. We also show self-cleaning capabilities using our soft robot driving by the square wave magnetic field (4 mT) at a high frequency of 30 Hz (Supplementary Fig. 22 and Supplementary Movie 15).

To investigate the dynamics of the robot actuation in an environment with maximum degrees of freedom, we develop a levitating four-arm robot (23 mg). The robot is positioned within a transparent glass encasing and levitated by an out-of-plane magnetic field (3.7 mT) from a permanent cylinder magnet. Applying an additional in-plane square wave magnetic field (50 Hz, 1.5 mT) causes the robot to deform and configure itself spatially (Supplementary Movie 16). In the initial 20 ms, the levitating robot bends itself around 30° CCW to balance with the force of gravity and the magnetic field. By reversing the direction of the in-plane magnetic field, the robot adjusts itself to perform horizontal levitation until 30 ms. The CW angle of inclination goes up to 45° at 40 ms and reverses to 0° again at 50 ms. This levitated motion is repeatable.

In summary, we here design and develop a series of untethered ultrafast and highly compliant small-scale soft-bodied robots based on our dynamic numerical models, and analyze their highly nonlinear dynamic behavior when subjected to simple alternating magnetic fields. The soft-bodied robots made from a soft magnetic elastomer membrane containing 70 wt% NdFeB particles show unprecedented dynamic performance. These ultrafast soft grippers are able to momentarily close around and release a living fly without harming it. Furthermore, two-arm rectangle-shaped robots perform 90° and 45° actuation at a high frequency up to 100 and 200 Hz, respectively. Our studies open up a cornucopia of potential applications for soft-bodied robots capable of transporting cargo, swimming, walking, and levitating. Tailoring the shape and dimensions of soft-bodied robots and exploring the excitation parameter space (spatial orientation, amplitude, and frequency of the magnetic field) will enable multi-behavioral patterns in soft actuators. The introduced dynamic numerical model will serve to guide the development of soft magnetically driven robots and their control strategies. This will endow such robots with the ability to accomplish sophisticated tasks and expand unexplored application fields that necessitate specific speeds. High-frequency muscle training in developmental biology and biomechanics, mechano-sensitivity studies of cells, experimental modeling in fluid mechanics, and compact energy harvesting systems will become accessible.

Methods

Magnetic soft robot preparation. The NdFeB microparticles powder (MQFP-14-12-20000, Magnequench Corp.) and PDMS (Sylgard 184, Dow Corning Corp.) are mixed uniformly in a 7:3 mass ratio for 20 min by magnetic stirring. Subsequently, Sylgard 184 curing agent (10 wt% of PDMS, Dow Corning Corp.) is added to the mixture and stirred for another 10 min, followed by a 5 min degassing process with a vacuum pump to remove air bubbles. The resulting composite is spin-coated (1000–12,000 rpm) on glass substrates coated with a thin sacrificial layer of PVA (PVA 115,000, VWR) for 60 s and cured on a hot plate (Harry Gestigkeit GmbH) at 70 °C for 2 h. The thickness of the composite membrane ranges from 7 to 210 μm (Supplementary Fig. 1a). Subsequently, the coated glass plates are immersed in deionized (DI) water for 2 h to remove the PVA layer, enabling a safe peeling process of the magnetic membranes from the glass substrates. Additional washing with DI water for 2 times is used to remove the residual PVA on the membrane surface. The following 30 s magnetization process is done with a 2.3 T out-of-plane magnetic field provided by a setup with two impulse electro magnetizers (EM2, Magness Corp.). The membranes are cut into various geometries by using a set of commercial casting modules, scissors, or a stencil cutter.

Soft robot characterization. Magnetic properties are characterized using a superconducting quantum interference magnetometer (Squid-VSM, Quantum Design Corp.). The thickness, as well as the internal distribution of the NdFeB particles of the prepared magnetic membranes, is investigated by cross-sectional imaging with a scanning electron microscope processed by focused ion beam etching. The sample preparation is done by fixing the membranes (2 × 5 mm²) on a Si wafer by a double-sided tape, followed by depositing a 6 ± 1-nm-thick conductive Cr layer to avoid charging of the surface. The mechanical properties of our soft robots are tested with a strain-stress test bench (TVM 5000N230N, Sauter GmbH) and the shear moduli determined by fitting the experimental data using a Neo-Hookean model.

Setup for demonstrations. An electromagnet (Lehrmittel Corp.) with two coils (diameter/coil: 115 mm and thickness/coil: 35 mm) is used to generate a magnetic field up to 10 mT with different oscillation frequencies for soft robot manipulation. A LabVIEW program is used to generate a control signal from a multifunction I/O

Device (USB-6211, National Instruments), to drive a bipolar power supply (BOP 20–10 M, Kepoc, Inc.). To produce specific magnetic fields for the experiments, the distance (70 mm) between the two magnetic coils is calibrated and set by a gaussmeter (HGM09s, Magnet System). The calculated inductance of the coils based on the measurement indicated below is about 4.5 mH. The resistance of the coil at DC current is about 1 Ω. The highest actuation frequency for driving our soft robots is up to 200 Hz, which is far from the self-resonance of the coil. The measurements are conducted using a KEYSIGHT E4990A ImpedanceMeter and a TENMA 72-7780 Multimeter. The coil is powered using a KEPCO BOP 20–10 M power supply, which has a maximum DC output range of ±20 V and an output response frequency up to 18 kHz (Supplementary Fig. 23). For the experiments in Figs. 1e, 2a, b, and 3, we use paper (Mondi Corp., Model Num. CCK0349) with a dry and rough surface as the substrate supporting our robots. This helps to lower the adhesion between the PDMS-based soft robots and the substrate.

This setup is used for the demonstrations in Figs. 1e, 2a, b, 3, 4c, d, e, and 5, and Supplementary Figs. 5–10, 13, 14, 15a–e, 20–22, and 24. For the experiments in Fig. 4a, b and Supplementary Figs. 3 and 18, we use commercial permanent magnets (HKCM Corp.), which can provide a maximum magnetic field of 25 mT, as stimuli for the robot.

Finite-element analysis. The results of the simulation are obtained with the commercial finite-element software Abaqus and a user-defined element subroutine. The Abaqus/Standard solver is used to simulate the dynamic behavior of magnetic soft robots. The Neo-Hookean model is used to predict the mechanical behavior of the magnetic material. For all simulations, the parameters of the magnetic materials (PDMS/NdFeB elastomer with 70 wt% of magnetic filler) are as follows, shear moduli $\mu = 250$ kPa (thickness = 210 μm) and $\mu = 115$ kPa (thickness = 80 μm), bulk moduli $K = 100\mu$, density $\rho = 2.13 \times 10^3$ kg m^{-3}, and magnetization $M = 123$ kA m^{-1}. The material parameters are obtained by fitting the bending test of a magnetic elastomer sheet with the simulation (Supplementary Fig. 24). Gravity is taken as 9.8 m s^{-2}. The bending degree in the simulation is defined as the angle formed by the tangential projection from the tip of the robot onto its initial resting plane; as seen from its side view.

Energy and power density. The energy density and power density are approximated by $\rho_E = 3\mu(\varepsilon_a)^2/2$ and $\rho_W = f\rho_E$, where ε_a is the actuated nominal strain and f is the actuated frequency[14]. We extract the maximum nominal strain from the finite-element result with different shapes of robots subjected to different actuation frequencies (5–200 Hz). Related results are given in Supplementary Fig. 12.

Imaging and video recordings. Slow-motion videos are taken by a high-speed camera (up to 2000 fps, Photron), all other videos and photos are taken with a DSLR camera (Canon 80D, 50 frames per second). All videos are post-processed by the software "Hitfilm express" and then the snapshots are extracted frame by frame.

Dynamic FEM model. The dynamic FEM is based on Zhao's subroutine[19] and uses an implicit direct integration method with the commercial Abaqus/Standard package. In the simulation, we consider the effect of gravity with the acceleration of gravity $g = 9.8$ m s^{-2}. The contact of the magnetic membrane to the ground is a hard contact with a friction factor equal to 0.5. We use Abaqus/standard solver to simulate the dynamic behavior. The solver uses the implicit Hilber–Hughes–Taylor operator for the integration of the equations of motion.

In the simulation of the flower-shaped robot (Supplementary Fig. 25a), the magnetic field is parallel to the direction of the magnetic moment (Supplementary Fig. 25b). When the applied magnetic field is along the magnetization direction of the magnetic membrane, there will be no torque to bend a petal (Supplementary Fig. 25c). Still, since the robot is never perfectly flat on the substrate, there are some folds at the end of the petals (Supplementary Fig. 25d). At the initial steps of the actuation process, the magnetic torque on the small folds will first lift the petals and then the full bending process follows. In the simulation, we add an initial vertical speed to the petals to account for such imperfections. To implement the needed imperfection and make the robot arm bendable, we apply a magnetic field of 2 mT (trigger load) along (1,1,1)-direction for 5 ms to the flower-shaped robot. The imperfection is shown in Supplementary Fig. 25e. Subsequently, we apply a magnetic field of 3 mT at 50 Hz along the (0,0,1)-direction.

The wavy path in Fig. 2d is related to the rotational angle changes of a one-arm trapezoid-shaped robot when it is actuated by an in-plane magnetic field of 20 Hz (also captured in the experiment, Supplementary Movies 4 and 7). Based on the simulations shown in Fig. 2d, we can predict more complex dynamics shown in Fig. 3a including "quantitative" details as those related to the estimation of the period of cross clapping. Furthermore, a plateau observed in the curve between 75 and 100 ms (Fig. 2d) corresponds to the flat state of the one-arm robot, which is present in the data shown in Fig. 3a.

Furthermore, we note that the observed irregularities in the simulation data are related to the fact that at the rotation angle of about 270° the robot touches a surface. The soft actuator does have a twist, which can be observed in the Supplementary Movie 7. In this respect, simulations do match the experimental findings.

With respect to the measurement of the rotation angle: the displacement is projected to a plane, which is perpendicular to the paper. In this representation, even a small twist results in rather large deviations leading to a complex shaped curve.

Data availability

Code availability

References
1. Rus, D. & Tolley, M. T. Design, fabrication and control of soft robots. *Nature* **521**, 467–475 (2015).
2. Laschi, C., Mazzolai, B. & Cianchetti, M. Soft robotics: technologies and systems pushing the boundaries of robot abilities. *Sci. Robot* **1**, eaah3690 (2016).
3. Wehner, M. et al. An integrated design and fabrication strategy for entirely soft, autonomous robots. *Nature* **536**, 451–455 (2016).
4. Wallin, T. J., Pikul, J. & Shepherd, R. F. 3D printing of soft robotic systems. *Nat. Rev. Mater.* **3**, 84–100 (2018).
5. Van Meerbeek, I. M., De, S. C. M. & Shepherd, R. F. Soft optoelectronic sensory foams with proprioception. *Sci. Robot* **3**, eaau2489 (2018).
6. Pelrine, R., Kornbluh, R., Pei, Q. & Joseph, J. High-speed electrically actuated elastomers with strain greater than 100%. *Science* **287**, 836–839 (2000).
7. O'Halloran, A., O'malley, F. & McHugh, P. A review on dielectric elastomer actuators, technology, applications, and challenges. *J. Appl. Phys.* **104**, 9 (2008).
8. Imboden, M. et al. High-speed mechano-active multielectrode array for investigating rapid stretch effects on cardiac tissue. *Nat. Commun.* **10**, 834 (2019).
9. Behl, M., Kratz, K., Zotzmann, J., Nochel, U. & Lendlein, A. Reversible bidirectional shape-memory polymers. *Adv. Mater.* **25**, 4466–4469 (2013).
10. Liu, Y., Shaw, B., Dickey, M. D. & Genzer, J. Sequential self-folding of polymer sheets. *Sci. Adv.* **3**, e1602417 (2017).
11. Liu, J. A. C., Gillen, J. H., Mishra, S. R., Evans, B. A. & Tracy, J. B. Photothermally and magnetically controlled reconfiguration of polymer composites for soft robotics. *Sci. Adv.* **5**, eaaw2897 (2019).
12. Zhao, Q. et al. An instant multi-responsive porous polymer actuator driven by solvent molecule sorption. *Nat. Commun.* **5**, 4293 (2014).
13. Laskar, A., Shklyaev, O. E. & Balazs, A. C. Designing self-propelled, chemically active sheets: Wrappers, flappers, and creepers. *Sci. Adv.* **4**, eaav1745 (2018).
14. Huang, H. -W., Sakar, M. S., Petruska, A. J., Pané, S. & Nelson, B. J. Soft micromachines with programmable motility and morphology. *Nat. Commun.* **7**, 12263 (2016).
15. Lu, H. et al. A bioinspired multilegged soft millirobot that functions in both dry and wet conditions. *Nat. Commun.* **9**, 3944 (2018).
16. Ren, Z., Hu, W., Dong, X. & Sitti, M. Multi-functional soft-bodied jellyfish-like swimming. *Nat. Commun.* **10**, 2703 (2019).
17. Kim, J. et al. Programming magnetic anisotropy in polymeric microactuators. *Nat. Mater.* **10**, 747–752 (2011).
18. Hu, W., Lum, G. Z., Mastrangeli, M. & Sitti, M. Small-scale soft-bodied robot with multimodal locomotion. *Nature* **554**, 81–85 (2018).
19. Kim, Y., Yuk, H., Zhao, R., Chester, S. A. & Zhao, X. Printing ferromagnetic domains for untethered fast-transforming soft materials. *Nature* **558**, 274–279 (2018).
20. Lum, G. Z. et al. Shape-programmable magnetic soft matter. *Proc. Natl Acad. Sci. USA.* **113**, 6007–6015 (2016).
21. Jeon, S. et al. Magnetically actuated microrobots as a platform for stem cell transplantation. *Sci. Robot.* **4**, eaav4317 (2019).
22. Xu, T., Zhang, J., Salehizadeh, M., Onaizah, O. & Diller, E. Millimeter-scale flexible robots with programmable three-dimensional magnetization and motions. *Sci. Robot.* **4**, eaav4494 (2019).
23. Ghosh, A. & Fischer, P. Controlled propulsion of artificial magnetic nanostructured propellers. *Nano Lett.* **9**, 2243–2245 (2009).
24. Fischer, P. & Ghosh, A. Magnetically actuated propulsion at low Reynolds numbers: towards nanoscale control. *Nanoscale* **3**, 557–563 (2011).
25. Erb, R. M., Martin, J. J., Soheilian, R., Pan, C. & Barber, J. R. Actuating soft matter with magnetic torque. *Adv. Funct. Mater.* **26**, 3859–3880 (2016).

26. Hines, L., Petersen, K., Lum, G. Z. & Sitti, M. Soft actuators for small-scale robotics. *Adv. Mater.* **29**, 1603483 (2017).

27. Lorenzo, D. et al. Formation and magnetic manipulation of periodically aligned microchains in thin plastic membranes. *J. Appl. Phys.* **112**, 083927 (2012).

28. Liu, Y. W., Zhan, Q. F. & Li, R. W. Fabrication, properties, and applications of flexible magnetic films. *Chinese Phys. B* **22**, 127502 (2013).

29. Vogtmann, D., St Pierre, R. & Bergbreiter, S. Magnetic actuation of thick film multi-material compliant mechanisms. *J. Micromech. Microeng.* **27**, 125021 (2017).

30. Zhang, J. & Diller, E. Untethered miniature soft robots: modeling and design of a millimeter-scale swimming magnetic sheet. *Soft Robot.* **5**, 761–776 (2018).

31. Cui, J. et al. Nanomagnetic encoding of shape-morphing micromachines. *Nature* **575**, 164–168 (2019).

32. Cianchetti, M., Laschi, C., Menciassi, A. & Dario, P. Biomedical applications of soft robotics. *Nat. Rev. Mater.* **3**, 143–153 (2018).

33. Nelson, B. J., Kaliakatsos, I. K. & Abbott, J. J. Microrobots for minimally invasive medicine. *Annu. Rev. Biomed. Eng.* **12**, 55–85 (2010).

34. Hu, C., Pané, S. & Nelson, B. J. Soft micro- and nanorobotics. *Annu. Rev. Control Rob. Auton. Syst.* **1**, 53–75 (2018).

35. Zhang, L. et al. Artificial bacterial flagella: fabrication and magnetic control. *Appl. Phys. Lett.* **94**, 064107 (2009).

36. Nguyen, V. Q. & Ramanujan, R. Novel coiling behavior in magnet-polymer composites. *Macromol. Chem. Phys.* **211**, 618–626 (2010).

37. Li, J. et al. Design and fabrication of microfluidic mixer from carbonyl iron–PDMS composite membrane. *Microfluid. Nanofluid.* **10**, 919–925 (2010).

38. Marchi, S., Casu, A., Bertora, F., Athanassiou, A. & Fragouli, D. Highly magneto-responsive elastomeric films created by a two-step fabrication process. *ACS Appl. Mater. Interfaces* **7**, 19112–19118 (2015).

39. Forterre, Y., Skotheim, J. M., Dumais, J. & Mahadevan, L. How the Venus flytrap snaps. *Nature* **433**, 421–425 (2005).

40. Yang, R., Lenaghan, S. C., Zhang, M. & Xia, L. A mathematical model on the closing and opening mechanism for venus flytrap. *Plant Signal. Behav.* **5**, 968–978 (2010).

41. Zhao, R. K., Kim, Y., Chester, S. A., Sharma, P. & Zhao, X. H. Mechanics of hard-magnetic soft materials. *J. Mech. Phys. Solids* **124**, 244–263 (2019).

42. Wang, L., Kim, Y., Guo, C. F. & Zhao, X. Hard-magnetic elastica. *J. Mech. Phys. Solids* **142**, 104045 (2020).

Acknowledgements

Author contributions

X.W., G.M., M.K., and D.M. designed the project and analyzed the results. X.W., G.M., J.G., G.S.C.B., M.K., and D.M. proposed the idea of this project. X.W. performed all experiments with the support from G.M., J.G., M.D., and R.I. J.G. developed the ultra-soft magnetic film. G.M. developed the dynamical model and performed the simulation. R.I. and T.K. wrote the LabVIEW code. L.B. and C.W. supported the robot characterization. X.W., G.M., D.W., M.K., and D.M. wrote the paper with input from all authors. J.F., M.K., and D.M. supervised the project.

Competing interests

The authors declare no competing interests.

Additional information

Supplementary information is available for this paper at https://doi.org/10.1038/s43246-020-00067-1.

Correspondence and requests for materials should be addressed to M.K. or D.M.

Reprints and permission information is available at http://www.nature.com/reprints

Publisher's note Springer Nature remains neutral with regard to jurisdictional claims in published maps and institutional affiliations.